Available online at www.sciencedirect.com

ScienceDirect

Nuclear Physics A 1000 (2020) 121785

NUCLEAR PHYSICS A

www.elsevier.com/locate/nuclphysa

Lifetime measurement and shell model description of negative parity states up to band-termination in ^{49}V

S. Mukhopadhyay [a,*], D.C. Biswas [a], L.S. Danu [a], R. Chakrabarti [a,1], U. Garg [b], S.K. Tandel [c], Y.K. Gupta [a], B.N. Joshi [a], G.K. Prajapati [a], B.V. John [a], S. Saha [d], J. Sethi [d], R. Palit [d]

[a] *Nuclear Physics Division, Bhabha Atomic Research Centre, Trombay, Mumbai, 400085, India*
[b] *Physics Department, University of Notre Dame, Notre Dame, IN 46556, USA*
[c] *UM-DAE Centre for Excellence in Basic Sciences, University of Mumbai, Mumbai 400098, India*
[d] *Dept. of Nuclear and Atomic Physics, TIFR, Mumbai 400005, India*

Received 21 January 2020; received in revised form 5 March 2020; accepted 19 March 2020
Available online 24 March 2020

Abstract

The yrast and a few of the yrare negative-parity states in the ^{49}V nucleus have been investigated employing the ^{27}Al(^{28}Si, α2p)^{49}V reaction. Most of the levels and the deexciting γ rays, reported earlier in ^{49}V, have been observed in this measurement using the Indian National Gamma Array (INGA) spectrometer. Mean lifetimes up to the band-terminating state have been extracted following Doppler Shift Attenuation Method (DSAM), and reduced transition probabilities have been deduced. Large Scale Shell Model (LSSM) calculations in the full fp shell employing various effective interactions with no restrictions imposed on the valence orbitals have been performed. The results that have been obtained from calculations are in fair agreement with the experimentally obtained values.

Keywords: Lifetime measurement; DSAM; Reduced transition probabilities; Shell-model calculations; Prolate and oblate shapes

* Corresponding author.
E-mail address: somm@barc.gov.in (S. Mukhopadhyay).
[1] Current affiliation: Department of Physics, University of Mumbai, Vidyanagari, Mumbai 400088, India.

https://doi.org/10.1016/j.nuclphysa.2020.121785
0375-9474/

1. Introduction

The $f_{7/2}$-shell nuclei, with proton and neutron numbers between the magic numbers 20 and 28, form an interesting island in the nuclide chart. The number of active valence particles in these nuclei is low enough to allow for a full shell model description [1–5] but, at the same time, large enough to develop collective behavior [6–8]. The middle of the $f_{7/2}$ shell is characterized by large deformations near the ground state; but, as one moves toward the end of the shell, the collective behavior is replaced by the single-particle effects. Information on lifetimes and the derived electromagnetic transition strengths of the levels can give a clear picture of the underlying phenomena, since the $B(M1)$ rates are sensitive to the single particle features, while the $B(E2)$ values are sensitive to rotational collectivity.

The level structures of the nuclei from ^{40}Ca to ^{56}Ni are well described within the framework of the shell model, and are dominated by the $(f_{7/2})^n$, and $(f_{7/2})^{n-r}\ (f_{5/2}p_{3/2}p_{1/2})^r$ configurations, where r = 1, 2, ... Yrast levels of the majority of $f_{7/2}$-shell nuclei follow the shell model pattern, exhibiting somewhat irregular level spacings, often with a marked discontinuity at the termination of the $f_{7/2}$ band of states at $J_{max} = J_{p\ max} + J_{n\ max} = \frac{1}{2}[Z(8-Z) + N(8-N)]$. This is particularly apparent in the nuclei near N or $Z = 20,\ 28$ where J_{max} is not large.

Several experimental and theoretical investigations have been carried out to study the interplay between single-particle and collective structures in $f_{7/2}$-shell nuclei. The ^{49}V nucleus, with three protons and six neutrons in the $f_{7/2}$ shell, is close to a small region of collectivity that exists at the middle of the $f_{7/2}$ shell. The yrast negative parity states are connected by strong E2 transitions up to spin, $J^\pi = \frac{23}{2}^-$. Side bands of positive parities in this nucleus were suggested to stem out of excitations from the sd shell [9,10]. It is to be noted that considerable amount of evidence has already been gathered for rotational structure in sd-shell nuclei.

High-spin states in ^{49}V nucleus were studied earlier by Cameron et al. employing ^{12}C(^{40}Ca, 3p)^{49}V reaction at a ^{40}Ca beam energy of 160 MeV and POLYTESSA array of sixteen escape-suppressed spectrometers [9]. A much detailed work on this nucleus, employing ^{28}Si(^{28}Si, α3p) reaction and EUROBALL IV + Recoil Filter Detector (RFD), has been reported recently, where the ^{49}V level scheme was extended up to an excitation energy of 13.1 MeV, with the observation of 21 new states [10]. However, the experimental data on mean lifetimes and reduced transition probabilities of higher excited states in ^{49}V remain rather sparse [11]. Therefore, a dedicated measurement employing Doppler Shift Attenuation Method (DSAM) was undertaken in the present investigation to deduce the aforesaid experimental observables. The results of this measurement, coupled with Large Scale Shell Model (LSSM) calculations, will be important to further explore the extent of collective and single-particle nature of states in nuclei near mid-$f_{7/2}$ shell.

2. Experiment, data analysis and results

The experiment was carried out at the Pelletron-Linac facility, TIFR, Mumbai. The ^{27}Al(^{28}Si, α2p) reaction was employed at a beam energy of 100 MeV to populate high-spin states in ^{49}V. The target consisted of a $\sim$750 μg/cm^2 thick Al foil with a 14.8 mg/cm^2-thick layer of Au backing. Deexciting γ rays were detected using the Indian National Gamma Array (INGA) spectrometer which comprised of twenty Compton-suppressed clover Ge detectors at the time of the measurement. The detector configuration of the array with respect to the beam direction was as follows: two each at 23°, and 115°; three each at 40°, 65°, 140° and 157°; four at 90°. A digital signal processing based data acquisition system [12], employing Pixie-16 modules from

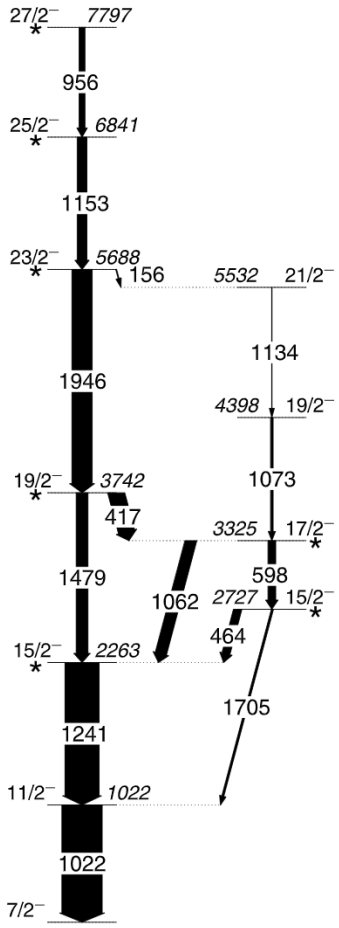

Fig. 1. Partial level scheme of ^{49}V, as obtained and relevant to this article. The levels for which lifetimes have been measured in the present investigation are marked with "$*$".

XIA-LLC, USA, was used to acquire two- and higher-fold time-stamped coincidence events, which were subsequently analyzed offline, using the RADWARE and LINESHAPE software packages [13–15].

The acquired data were initially sorted into conventional symmetric $\gamma - \gamma$ and 3-dimensional $\gamma - \gamma - \gamma$ cube. Multiple asymmetric (angle dependent) $\gamma - \gamma$ matrices were also constructed to generate gated spectra at different angles for LINESHAPE analysis. Most of the γ transitions that were reported earlier have been observed in the present data. A partial level scheme, as deduced from the present data, is shown in Fig. 1. It should be noted that only a part of the deduced level scheme which is relevant to the present article and the discussion therein, is depicted in Fig. 1. The relative intensities and branching ratios of the observed transitions have been measured, and were subsequently fed in LINESHAPE analysis. It is worth noting that most of the branching ratios, as obtained from the present data, are in reasonable agreement with the previous measurement [10].

2.1. LINESHAPE analysis

Doppler broadened lineshapes were clearly observed in forward and backward angle detectors for almost all the transitions in Fig. 1 above $J^{\pi} = \frac{11}{2}^{-}$ ($E_x = 1022$ keV). Energy gated spectra projected on forward, transverse, and the complementary backward angles were used to extract the mean lifetimes of the levels (marked with "$*$" in Fig. 1). The spectra with energy gates on 1022-keV and 1241-keV transitions were summed together to obtain sufficient counts under a peak and its Doppler broadened region at each angle. For some transitions, depopulating the lower spin states, spectrum with energy gate on only the 1022-keV transition was used. In case of the 1241-keV energy gate, the full peak shape that includes the stopped component and the shifted part of it, was taken into account. This eliminated a possible influence in the subsequent lifetime analysis following DSAM that could be introduced by omission of the tails of the peak line shape containing the fast time component of the gating transition.

The LINESHAPE software package by Wells and Johnson was used for the analysis [15]. The 1073-keV transition, depopulating the $\frac{19}{2}^{-}_{2}$ level at $E_x = 4398$ keV, has Doppler broadened lineshapes that overlap with those of the much stronger 1062-keV transition. Hence, the mean lifetime of the $\frac{19}{2}^{-}_{2}$ level could not be extracted unambiguously. Furthermore, the mean lifetime of the $\frac{21}{2}^{-}$ level could not be determined due to insufficient count for the 1134-keV transition when detectors in only forward and backward angles were considered for projection. The aforesaid analysis, taking three angles at a time, was mostly done using spectra projected on 65°, 90° and 115° angles. However, for certain transitions, data from another subset of angles (*viz.* 40°, 90° and 140°) were also analyzed, and the results were found to be in agreement within the experimental uncertainty.

In the LINESHAPE analysis, electronic stopping powers were calculated following the heavy-ion stopping power theory by Ziegler et al. [16]. A total of 10000 Monte Carlo simulations of velocity history of the recoiling nuclei traversing the target (Al) and backing material (Au) were generated in time steps of 0.0001 ps. The velocity histories of the recoil nuclei, thus created, were later converted into time-dependent velocity profiles as seen by clover detectors at a particular angle.

To begin with, side feeding into each negative parity state (marked with "$*$" in Fig. 1) was modeled as a five-transition rotational band with dynamic moment of inertia equivalent to that of the ground state band. The in-band transition quadrupole moments, side-feeding transition quadrupole moments, peak parameters, contaminant peak- and background parameters were allowed to vary. Starting with the transition at maximum excitation energy in a sequence, the spectra at all the three angles were fitted simultaneously for a particular transition. The stopped contaminant peak- and background parameters were then fixed, and the minimum χ^2 was obtained for a transition. It may be noted that for the 956-keV and 1153-keV transitions, only forward and transverse spectra were fitted simultaneously as the spectra in the backward angles for these two transitions were highly contaminated.

The in-band and side-feeding lifetimes, thus obtained, were used in the next lower level of the sequence as the effective feeding time parameters to that level. After obtaining the individual best-fits of the peaks, the entire sequence was included in a global fit with independently variable in-band and side-feeding lifetimes for each transition [17,18]. Representative examples of DSAM fits to the data are presented in Figs. 2, 3, and the extracted mean lifetimes of the levels are summarized in Table 1. Uncertainties in the lifetime values were determined from the behavior

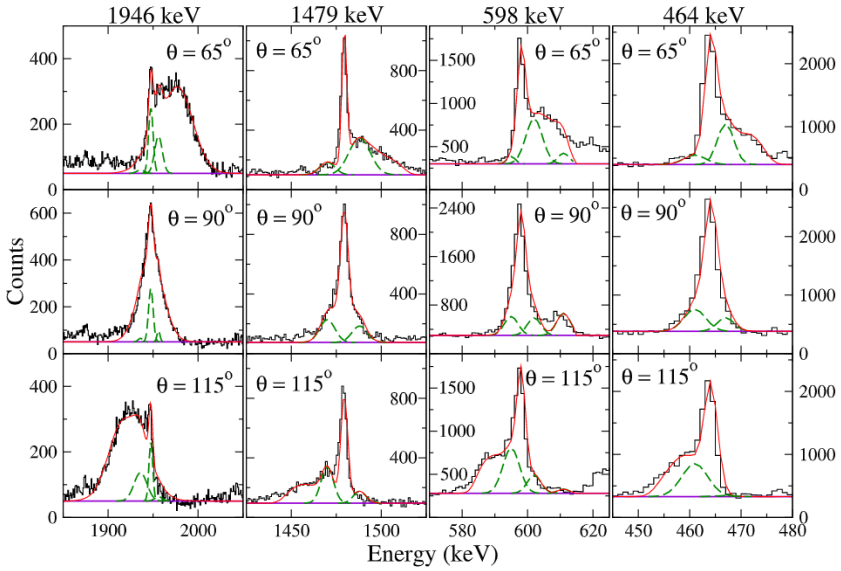

Fig. 2. Experimental data and associated Doppler broadened line-shape fits for γ-ray transitions in the negative parity structure of ^{49}V.

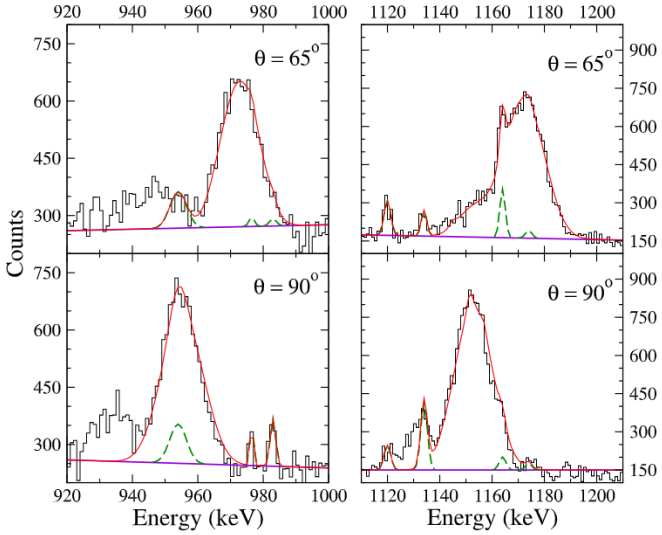

Fig. 3. Experimental data and associated Doppler broadened line-shape fits for the top two $\Delta J = 1$ γ-ray transitions leading to the band-terminating $27/2^-$ state in ^{49}V. Left panel: $E_\gamma = 956$ keV ($27/2^- \rightarrow 25/2^-$); Right panel: $E_\gamma = 1153$ keV ($25/2^- \rightarrow 23/2^-$).

of χ^2-fit in the vicinity of the minimum. It should be noted that the systematic errors associated with the modeling of the stopping power can be as large as 10-15%. However, those are not included in the quoted errors in Table 1.

Table 1
Energy levels, corresponding depopulating γ ray transition energies, relative intensities of γ transitions, spins and parities of the initial and final levels, mean lifetimes and deduced E2 transition rates as obtained from the analysis of the data. Mean lifetimes and $B(E2)$ values of the levels, obtained from shell model calculations, are also tabulated in columns immediately after the respective columns with experimental values for comparison.

E_x^a (keV)	E_γ^b (keV)	I_γ (%)	$J_i^\pi \rightarrow J_f^\pi$	$\tau_{expt.}$ (ps)	τ_{SM} (ps)	$B(E2)_{expt.}$ (e^2 fm^4)	$B(E2)_{SM}$ (e^2 fm^4)
1022	1021.6	>118.0	$\frac{11}{2}^- \rightarrow \frac{7}{2}^-$	5.1(1.0)[1]	3.73[k],4.49[g],1.50[f]	144(28)[1]	182.6[k],176.9[g],215.5[f]
2263	1241.2	100.0	$\frac{15}{2}^-_1 \rightarrow \frac{11}{2}^-$	0.92(14)	1.40[k],2.94[g],1.87[f]	301(46)	165.0[k],136.7[g],117.5[f]
				$0.93^{+0.55}_{-0.28}$[1]		297(128)[1]	
2727	1705.3	5.9	$\frac{15}{2}^-_2 \rightarrow \frac{11}{2}^-$	0.41(6)	0.23[k],0.32[g],0.38[f]	110.3(16)	40.3[k],63.2[g],125.2[f]
				$0.35^{+0.15}_{-0.11}$[1]		161.6(41)[1]	
	464.1	23.9	$\frac{15}{2}^-_2 \rightarrow \frac{15}{2}^-_1$				
3325	598.1	22.7	$\frac{17}{2}^- \rightarrow \frac{15}{2}^-_2$	0.08(1)	0.07[k],0.07[g],0.05[f]		
	1062.4	33.7	$\frac{17}{2}^- \rightarrow \frac{15}{2}^-_1$				
3742	1479.3	34.4	$\frac{19}{2}^-_1 \rightarrow \frac{15}{2}^-_1$	0.38(4)	0.42[k],0.62[g],0.24[f]	127.2(13)	89.4[k],77.2[g],38.1[f]
	416.8	48.4	$\frac{19}{2}^-_1 \rightarrow \frac{17}{2}^-$				
4398	1072.9	7.5	$\frac{19}{2}^-_2 \rightarrow \frac{17}{2}^-$		0.03[k],0.03[g],0.04[f]		
5532	1133.6		$\frac{21}{2}^- \rightarrow \frac{19}{2}^-_2$		0.06[k],0.11[g],0.02[f]		
5688	1946.1	59.3	$\frac{23}{2}^- \rightarrow \frac{19}{2}^-_1$	0.31(3)	0.20[k],0.27[g],0.22[f]	90.5(9)	98.7[k],93.2[g],94.5[f]
	156.6	2.5	$\frac{23}{2}^- \rightarrow \frac{21}{2}^-$				
6841	1152.9	28.4	$\frac{25}{2}^- \rightarrow \frac{23}{2}^-$	0.09(2)	0.04[k],0.04[g],0.03[f]		
7797	955.5	17.2	$\frac{27}{2}^- \rightarrow \frac{25}{2}^-$	< 0.05(1)	0.02[k],0.03[g],0.03[f]		

[a] The level energies (E_x) are rounded off to the nearest integer values. Uncertainty for a level energy can be determined by adding the uncertainties in the γ-ray energies leading to that level. The highest uncertainty, thus calculated, is ~0.6 keV (for $E_x = 7797$ keV).
[b] Uncertainties in γ-ray energies (E_γ) are 0.2 keV for most of the transitions.
[1] Ref. [11].
[k] Using *KB3G* effective interaction; [g] using *GXPF1A* effective interaction; [f] using *FPD6* effective interaction.

3. Discussion

Large Scale Shell Model (LSSM) calculations with the full fp shell as the model space have been performed to interpret the experimental observations, and to look for exotic behaviors such as shape change and the evolution of collectivity as a function of spin along the yrast sequence. The code NuShellX@MSU [19] was used in conjunction with the various standard effective interactions in the fp model space, such as, $KB3G$, $FPD6$, as well as the more recent $GXPF1A$ in the present work. The monopole-modified interaction $KB3$ [20], as well as its shell-gap readjusted version $KB3G$ [3], appear to be quite successful in the lower fp shell nuclei (A≤52). On the other hand, the $FPD6$ [21] interaction assumes an analytic two-body potential, with parameters determined from fits to the experimental data in the A = 41~49 nuclei. The recently developed $GXPF1A$ [22] interaction was derived from a microscopic interaction where a subset of the 195 Two Body Matrix Elements ($TBME$) and 4 Single Particle Energies (SPE) were determined by fitting the observed energy data for 699 energy levels from 87 nuclei (47≤A≤66).

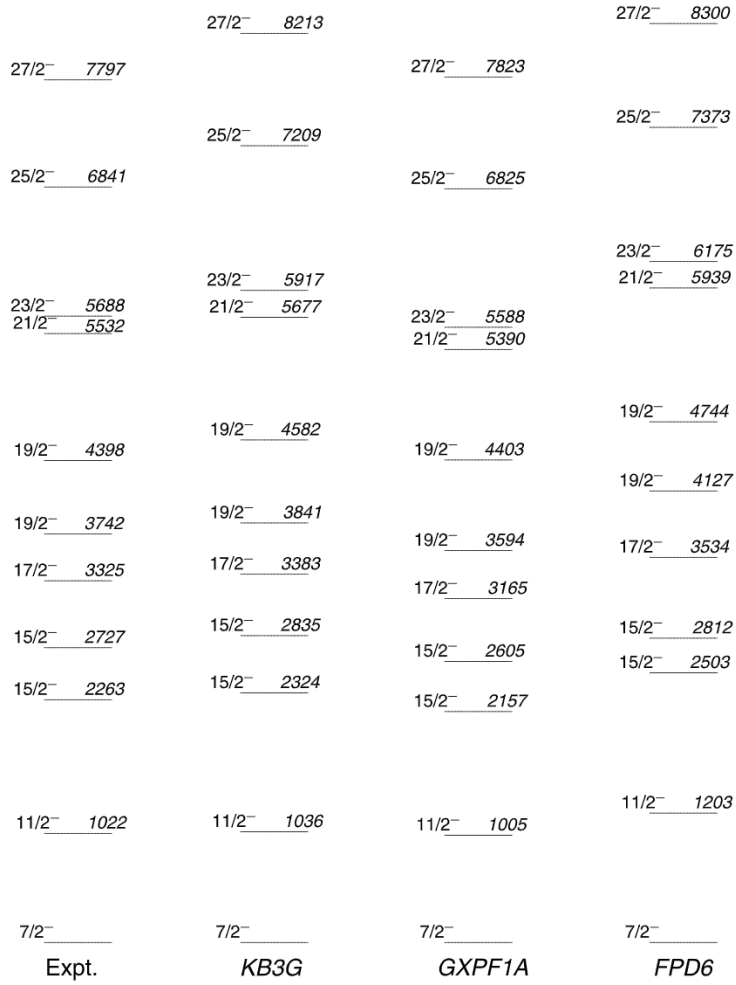

Fig. 4. Comparison of energy levels with those obtained from Large Scale Shell Model (LSSM) calculations employing *KB3G*, *GXPF1A* and *FPD6* effective interactions. See text for more details.

The present calculations have been carried out in the full fp shell ($f_{7/2}$ $p_{3/2}$ $f_{5/2}$ $p_{1/2}$) outside the ^{40}Ca core. The proton (e_p) and neutron (e_n) effective charges were adopted as 1.5 and 0.5, respectively. It is to be noted that due to the availability of High Performance Computing System (HPCS) at Nuclear Physics Division, BARC, neither any truncation of the full fp model space was necessitated nor any restriction was imposed on the allowed number (minimum and maximum) of a particular type of nucleon (neutron/proton) in a certain orbital during the course of calculations. In fact, the results from such calculations employing the aforesaid three different interactions have been compared for the first time in case of ^{49}V nucleus in order to get a clear picture of their applicability (or usefulness) in case of $N = Z + 3$ nuclei around the middle of $f_{7/2}$ shell.

The experimental excitation energies for natural parity states in ^{49}V have been compared to the theoretical predictions in Fig. 4 for the three aforementioned effective interactions. As seen from the figures, the agreement between the experimental and theoretical excitation energies is

quite reasonable. The $\frac{11}{2}^-$ state is well reproduced by both the $KB3G$ and $GXPF1A$ effective interactions. Higher excited states from $\frac{15}{2}^-_1$ ($E_x = 2263$ keV) to $\frac{19}{2}^-_1$ ($E_x = 3742$ keV) are better reproduced by the $KB3G$ interactions, whereas the $GXPF1A$ always underestimates the excitation energies of these set of levels. However, the $\frac{19}{2}^-_2$ state in the three quasiparticle band is very well reproduced by the $GXPF1A$ effective interaction with a difference between the experimental and calculated levels being only 5 keV. The calculated energies for the yrast $\frac{21}{2}^-$ level with both $KB3G$ and $GXPF1A$ effective interactions are in fair agreement with the experimental value. However, whereas the $KB3G$ interaction overestimates the excitation energy for this level ($|\Delta E| = 145$ keV), the $GXPF1A$ underestimates it with an almost equal energy difference ($|\Delta E| = 142$ keV). Finally, for the states beyond $\frac{21}{2}^-$, the $GXPF1A$ effective interaction appears to be a much better choice, and reproduces the experimental excitation energies very well, even to the extent of $|\Delta E_{Expt.-Cal.}| < 27$ keV for the band-terminating state and the one that precedes it. It is worth noting that in the present calculation scheme with no restrictions imposed on either the model space or the valence particles, the results obtained employing the $FPD6$ interaction were way off for almost all the levels compared to those obtained employing the other two interactions. The average particle occupancies of the predicted negative-parity states for all the three effective interactions are listed in Table 2.

The side band that starts at the $\frac{15}{2}^-_2$ state at 2726.9 keV has already been interpreted as a three quasiparticle structure [5,10]. The strong overlap of the associated wave functions of the states in this band with those in the ground state band is further supported by the data in Table 2. The particle occupancies for the $\frac{19}{2}^-_1$ level match more closely with those for the $\frac{17}{2}^-$ level instead of the $\frac{15}{2}^-_1$ level. This explains that for the $\frac{19}{2}^-_1$ level at $E_x = 3742$ keV, the 416.8 keV transition is preferred over the 1479.3 keV transition by a factor of 1.6, in agreement with the experimentally measured factor of 1.4 (Table 1). Similar arguments explain that for the $\frac{17}{2}^-$ level at 3325 keV, the inter-band 1062.4 keV transition is preferred over the intra-band 598.1 keV transition. The factor of preference as obtained in the calculation is 2.3, which is in reasonable agreement with the experimentally measured factor of 1.5 (Table 1).

The calculated spectroscopic quadrupole moment, Q_s is related to the intrinsic quadrupole moment, Q_0, by the formulae

$$Q_s = Q_0 \frac{3K^2 - I(I+1)}{(I+1)(2I+3)} \tag{1}$$

For the usual ground state of nuclei with $I = K$, the formulae simplifies to

$$Q_s = Q_0 \frac{I(2I-1)}{(I+1)(2I+3)} \tag{2}$$

Under the assumption of constant-charge distribution within the nucleus, the intrinsic quadrupole moment determines the general shape of the nucleus. Whereas a positive Q_0 corresponds to a nucleus with a prolate shape like a rugby football or cigar, a negative value of the same signifies a nucleus with oblate disk-like shape. The intrinsic quadrupole moment is zero for spherical nuclei.

It should be noted that it is not true, in general, that the shape of a nucleus (prolate/oblate) is determined from the sign of the spectroscopic quadrupole moment. As is evident from Eq. (1), for rotational states with total angular momentum I, large in comparison with K (the projection of I upon the symmetry axis of the nucleus), the spectroscopic quadrupole moment is negative for a nucleus with prolate deformation (*viz.* positive Q_0).

Table 2
Average particle occupancies of negative parity states in ^{49}V from Large Scale Shell Model (LSSM) calculations assuming ^{40}Ca core and no restriction on occupation of orbitals by the valence nucleons in the full fp valence space.

J^π	E_x (keV)	$\nu f_{7/2}$	$\nu p_{3/2}$	$\nu f_{5/2}$	$\nu p_{1/2}$	$\pi f_{7/2}$	$\pi p_{3/2}$	$\pi f_{5/2}$	$\pi p_{1/2}$	Eff. Int.
$\frac{11}{2}^-$	1022	5.4020	0.2897	0.2450	0.0628	2.7046	0.1566	0.1150	0.0237	*KB3G*
		5.4944	0.2993	0.1580	0.0480	2.7564	0.1698	0.0604	0.0135	*GXPF1A*
		5.1530	0.4492	0.3177	0.0797	2.5542	0.2696	0.1416	0.0347	*FPD6*
$\frac{15}{2}^-_1$	2263	5.4847	0.2289	0.2340	0.0526	2.7299	0.1211	0.1264	0.0228	*KB3G*
		5.5827	0.2222	0.1566	0.0387	2.7722	0.1288	0.0827	0.0165	*GXPF1A*
		5.3059	0.3411	0.2876	0.0649	2.5712	0.2218	0.1688	0.0382	*FPD6*
$\frac{15}{2}^-_2$	2727	5.4750	0.2535	0.2176	0.0538	2.6817	0.1658	0.1242	0.0284	*KB3G*
		5.5170	0.2850	0.1531	0.0450	2.7053	0.1960	0.0814	0.0174	*GXPF1A*
		5.2103	0.4174	0.2969	0.0748	2.5360	0.2763	0.1493	0.0383	*FPD6*
$\frac{17}{2}^-$	3325	5.5811	0.1918	0.1844	0.0424	2.7506	0.1116	0.1141	0.0237	*KB3G*
		5.6252	0.2074	0.1298	0.0374	2.7892	0.1220	0.0736	0.0151	*GXPF1A*
		5.3888	0.3141	0.2379	0.0588	2.5995	0.2139	0.1486	0.0380	*FPD6*
$\frac{19}{2}^-_1$	3742	5.5776	0.1776	0.2073	0.0373	2.7882	0.0811	0.1100	0.0206	*KB3G*
		5.6434	0.1756	0.1526	0.0283	2.8413	0.0872	0.0567	0.0149	*GXPF1A*
		5.4417	0.2603	0.2503	0.0474	2.6988	0.1489	0.1212	0.0311	*FPD6*
$\frac{19}{2}^-_2$	4398	5.5239	0.2180	0.1994	0.0585	2.7613	0.1082	0.1131	0.0173	*KB3G*
		5.5801	0.2364	0.1308	0.0526	2.7976	0.1264	0.0643	0.0118	*GXPF1A*
		5.2957	0.3808	0.2521	0.0713	2.6598	0.1897	0.1247	0.0259	*FPD6*
$\frac{21}{2}^-$	5532	5.6457	0.1599	0.1618	0.0325	2.8420	0.0651	0.0748	0.0182	*KB3G*
		5.7294	0.1454	0.1021	0.0231	2.8865	0.0596	0.0424	0.0116	*GXPF1A*
		5.4319	0.3015	0.2133	0.0532	2.6923	0.1701	0.1017	0.0358	*FPD6*
$\frac{23}{2}^-$	5688	5.6688	0.1263	0.1786	0.0262	2.8597	0.0469	0.0832	0.0102	*KB3G*
		5.7343	0.1234	0.1239	0.0184	2.8917	0.0494	0.0520	0.0069	*GXPF1A*
		5.5428	0.1998	0.2222	0.0351	2.7968	0.0908	0.0964	0.0160	*FPD6*
$\frac{25}{2}^-$	6841	5.6619	0.1209	0.1877	0.0294	2.8246	0.0422	0.1241	0.0090	*KB3G*
		5.7035	0.1364	0.1377	0.0224	2.8374	0.0510	0.1039	0.0077	*GXPF1A*
		5.5404	0.1872	0.2359	0.0363	2.7789	0.0762	0.1293	0.0155	*FPD6*
$\frac{27}{2}^-$	7797	5.7549	0.0985	0.1264	0.0201	2.9434	0.0165	0.0366	0.0036	*KB3G*
		5.8445	0.0830	0.0622	0.0103	2.9718	0.0161	0.0105	0.0015	*GXPF1A*
		5.7018	0.1372	0.1379	0.0230	2.9279	0.0296	0.0368	0.0057	*FPD6*

The intrinsic quadrupole moment of deformed nuclei, Q_0, is related to the reduced $E2$ γ-ray transition probability, $B(E2)$, for rotational transitions by the following expression:

$$B(E2; I_i \rightarrow I_f) = \frac{5}{16\pi} e^2 Q_0^2 \langle I_i K 20 | I_f K \rangle^2 \tag{3}$$

The term $\langle I_i K 20 | I_f K \rangle$ in Eq. (3) is the Clebsch-Gordan coefficient. Q_0 is also related to the deformation parameter β by the following relation:

$$Q_0 = 1.09 Z A^{2/3} \beta (1 + 0.158\beta) \text{ e fm}^2 \tag{4}$$

The constant coefficient inside the bracket in Eq. (4) has been adopted differently by some authors in the past [5], and therefore, we define the parameter $\beta^* = \beta(1 + 0.158\beta)$ for further use in this article. To infer the evolution of shape as we go higher in spins up to the band-terminating $\frac{27}{2}^-$ state in ^{49}V, the prescription that was followed in Ref. [5], has been adopted here. The ^{49}V nucleus starts with a negative Q_s value in its ground state which further increases in the negative

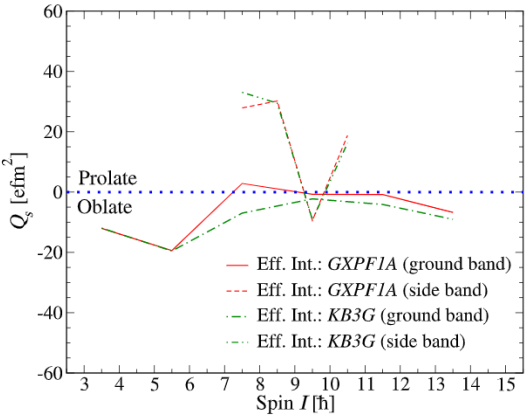

Fig. 5. Evolution of spectroscopic quadrupole moment, Q_s, with spin along the negative parity ground band and three quasiparticle side band in ^{49}V following Large Scale Shell Model calculations.

Table 3
Spectroscopic quadrupole moments, Q_s, for negative parity states in ^{49}V following shell model calculations.

J^π	E_x (keV)	Q_s (e fm^2)	
		KB3G	*GXPF1A*
$\frac{7}{2}^-$	0	-11.99	-12.03
$\frac{11}{2}^-$	1022	-19.54	-19.38
$\frac{15}{2}^-_1$	2263	-6.98	2.83
$\frac{15}{2}^-_2$	2727	33.06	27.9
$\frac{17}{2}^-$	3325	29.47	30.2
$\frac{19}{2}^-_1$	3742	-2.25	-0.74
$\frac{19}{2}^-_2$	4398	-9.25	-9.45
$\frac{21}{2}^-$	5532	16.26	18.79
$\frac{23}{2}^-$	5688	-4.11	-0.80
$\frac{25}{2}^-$	6841	-8.08	-7.86
$\frac{27}{2}^-$	7797	-9.03	-6.76

direction for the $\frac{11}{2}^-$ state (Fig. 5, Table 3). This is consistent with its particle-like nature, to which an oblate noncollective shape pertains. The ground state band is crossed by a $K^\pi = \frac{15}{2}^-_2$ band. The $\frac{15}{2}^-_2$ bandhead state of this side band and its member with spin, $J^\pi = \frac{17}{2}^-$, have Q_s values of 33.06 and 29.47 e fm^2, respectively ($KB3G$) (Table 3). The large positive values of Q_s for these states in the side band point toward their hole-like nature which pertains to a prolate noncollective shape. In a semiclassical description, $Q_s = Q_0$, and hence, $\beta^* \simeq 0.10, 0.09$ have been derived from Eq. (4) for the $\frac{15}{2}^-_2$ and $\frac{17}{2}^-$ states, respectively. The crossing between the two bands results in lowering the Q_s value (*i.e.*, pulling it up toward the positive side) for the ground band (Fig. 5). On the other hand, the side band makes a sudden transition toward noncollective oblate shape (at spin, $J^\pi = \frac{19}{2}^-$) only to return to its hole-like nature at spin, $J^\pi = \frac{21}{2}^-$. The

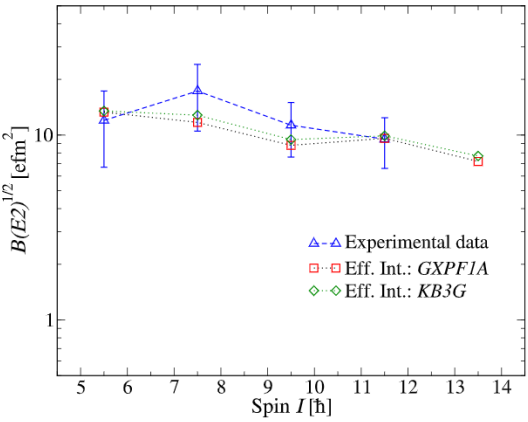

Fig. 6. Depiction of experimental $B(E2)$ values with spin along the negative parity ground band in ^{49}V, and their comparison with those obtained following shell model calculations.

sudden dip in the Q_s value at spin, $J^\pi = \frac{19}{2}^-$ was reported earlier following truncated shell model calculations [5]. However, the magnitude (~ 40 e fm^2) of this dip at spin, $J^\pi = \frac{19}{2}^-$, and its subsequent partial recovery (by ~ 25 e fm^2) at spin, $J^\pi = \frac{21}{2}^-$, would require further investigation. At the termination of the ground band, the Q_s value is -6.76 e fm^2 ($GXPF1A$), indicating that the hole-like shape prevails (Fig. 5, Table 3).

The transition probabilities computed from the associated wave functions are compared with the experimental values in Fig. 6. The square roots of the $B(E2)$ values in the ground band are plotted because those are approximately linearly proportional to the deformation like the Q_0 values. It is evident that the experimental values are in fair agreement with the calculated numbers within the experimental uncertainties. The sharp increase in the experimental $B(E2)$ value for the $\frac{15}{2}^-_1$ state points toward the strong influence of the overlapping orbitals for the low lying states of the $K^\pi = \frac{15}{2}^-_2$ band, and thereby, renders a sudden enhancement of noncollective prolate deformation to the $\frac{15}{2}^-$ state in the ground band (Fig. 6). The $B(E2)$ values, and in turn, the deformation of the ground band follow a smooth decreasing trend thereafter, with the calculated value of $\beta^* = 0.02$ ($GXPF1A$) at the band terminating state.

4. Summary

Lifetime measurements have been performed for the natural parity yrast and yrare states in the $N = Z + 3$, $f_{7/2}$-shell ^{49}V nucleus, employing Doppler Shift Attenuation Method (DSAM). Mean lifetimes of the states with spin, $J^\pi > \frac{15}{2}^-_2$, and up to the band-terminating state, have been extracted for the first time. The reduced E2 transition probabilities, which give a measure of the extent of collectivity near the middle of the $1f_{7/2}$-shell, have been deduced. Large Scale Shell Model (LSSM) calculations have been performed in the full fp valence space employing $KB3G$, $FPD6$ and $GXPF1A$ effective interactions, with no restrictions imposed on the occupation of the orbitals. This demonstrates a comparative performance of multiple effective interactions for an $f_{7/2}$-shell nucleus under the aforementioned condition. Average particle occupancies for the negative parity levels in ^{49}V, as predicted by LSSM calculations, are presented in detail.

The spectroscopic quadrupole moments obtained from the shell model calculations, have been discussed under the contexts of collectivity and non-collectivity along the ground band. The crossing between the ground band and the three quasiparticle side band supports the evolution of Q_s with spin. It'll be interesting to investigate the non-natural parity states in this nucleus following the same prescription.

Declaration of competing interest

The authors declare that they have no known competing financial interests or personal relationships that could have appeared to influence the work reported in this paper.

Acknowledgements

The authors thank and gratefully acknowledge the INGA Collaboration for making the detectors available during this measurement. Thanks are due to all the operation staff in the Pelletron-Linac facility at TIFR, Mumbai, for their effort in running the accelerator. Special thanks to Mr. Ajit Mahadkar, Target Laboratory, TIFR, for preparing the target on a short notice. This work was supported in part by the Department of Science and Technology, Government of India [grant number IR/S2/PF-03/2003-II]; and the U.S. National Science Foundation [grant numbers PHY-1068192, PHY-1713857].

References

[1] E. Caurier, A.P. Zuker, A. Poves, G. Martínez-Pinedo, Phys. Rev. C 50 (1994) 225.
[2] G. Martínez-Pinedo, A.P. Zuker, A. Poves, E. Caurier, Phys. Rev. C 55 (1997) 187.
[3] A. Poves, J. Sánchez-Solano, E. Caurier, F. Nowacki, Nucl. Phys. A 694 (2001) 157.
[4] F. Brandolini, et al., Nucl. Phys. A 642 (1998) 387.
[5] F. Brandolini, C.A. Ur, Phys. Rev. C 71 (2005) 054316.
[6] F. Brandolini, et al., Phys. Rev. C 66 (2002) 024304.
[7] G. Martínez-Pinedo, A. Poves, L.M. Robledo, E. Caurier, F. Nowacki, J. Retamosa, A. Zuker, Phys. Rev. C 54 (1996) R2150.
[8] J.A. Cameron, et al., Phys. Lett. B 387 (1996) 266.
[9] J.A. Cameron, M.A. Bentley, A.M. Bruce, R.A. Cunningham, W. Gelletly, H.G. Price, J. Simpson, D.D. Warner, A.N. James, Phys. Rev. C 44 (1991) 1882.
[10] D. Rodrigues, et al., Phys. Rev. C 92 (2015) 024323.
[11] B. Haas, J. Chevallier, J. Britz, J. Styczen, Phys. Rev. C 11 (1975) 1179.
[12] R. Palit, et al., Nucl. Instrum. Methods A 680 (2012) 90.
[13] D.C. Radford, Nucl. Instrum. Methods A 361 (1995) 297.
[14] http://radware.phy.ornl.gov/.
[15] J. Wells, N. Johnson, Oak Ridge National Laboratory, Report No. ORNL-6689, 1991 (unpublished).
[16] J.F. Ziegler, J.P. Biersack, U. Littmark, The Stopping and Range of Ions in Solids, Pergamon, New York, 1985.
[17] S. Mukhopadhyay, et al., Phys. Rev. C 78 (2008) 034311.
[18] S. Mukhopadhyay, et al., Phys. Rev. C 83 (2011) 044311.
[19] B.A. Brown, W.D.M. Rae, Nucl. Data Sheets 120 (2014) 115.
[20] A. Poves, A. Zuker, Phys. Rep. 70 (1981) 235.
[21] W.A. Richter, M.G. Van Der Merwe, R.E. Julies, B.A. Brown, Nucl. Phys. A 523 (1991) 325.
[22] M. Honma, T. Otsuka, B.A. Brown, T. Mizusaki, Eur. Phys. J. A 25 (2005) 499.